Modeling Acoustic Wavefields from Moving Sources in the Presence of a Time-varying Free-surface Boundary

Khalid Almuteri, Jeffrey Shragge & Paul Sava

Center for Wave Phenomena and Dept. of Geophysics, Colorado School of Mines, Golden CO 80401
email kalmuteri@mines.edu

ABSTRACT

Marine vibrators are increasingly being recognized as a viable alternative to seismic air guns for ocean-bottom acquisition due to their ability to generate more low-frequency content and their more limited impact on marine wildlife. However, their use introduces processing challenges, such as the Doppler effect and time-dependent source-receiver offsets, which are absent from conventional air-gun acquisition. Additionally, the time-varying nature of the sea surface during acquisition poses further challenges. To accurately account for source motion and time-varying sea surface effects in seismic data processing, we develop a reliable and robust tool for numerical experimentation. We use a mimetic finite-difference method in a generalized coordinate system to model the full acoustic wavefield triggered by a moving source in the presence of a time-varying sea surface. Our approach uses a coordinate transformation to map an irregular physical domain (in Cartesian coordinates), which tracks the source movement and conforms to the irregular time-varying sea surface, to a regular computational domain (in generalized coordinates). We formulate this coordinate transformation such that both coordinate systems conformally match below the ocean-bottom level. Numerical examples demonstrate that this approach is accurate and stable, even for an unrealistically exaggerated sea state. This computational tool is not limited to modeling, but can also be used to develop advanced processing techniques for marine vibrator data, such as imaging and inversion.

1 INTRODUCTION

Conventional ocean-bottom data processing assumes stationary sources with a short excitation duration. Consequently, source-side ghost reflections can be explained by an effective static rough sea surface, whereas receiver-side ghost reflections are explained by a time-varying sea surface. In marine vibrator acquisition, where sources are continuously moving and sweeping for a considerable period (e.g., 5 s), such assumptions are no longer true because source motion introduces offset- and time-dependent frequency shifts to the data (Dragoset, 1988; Schultz et al., 1989; Hampson and Jakubowicz, 1995), and source-receiver offsets become time-dependent. The long duration of the source function requires using a time-varying sea-surface model to accurately predict source-side ghost reflections. Therefore, accounting for moving sources and time-varying sea surfaces in seismic data processing is necessary to avoid introducing artifacts in the marine vibrator processed data.

Marine vibrators are advantageous over conventional seismic air guns for environmental and geophysical reasons. First, marine vibrators have a limited impact on marine wildlife life compared to conventional seismic air guns (Smith and Jenkerson, 1998). Additionally, marine vibrators can provide richer low-frequency content (Dellinger et al., 2016; Guitton et al., 2021) and enable a versatile control over the source signature, where the phase can be specified independently for each output frequency (Laws et al., 2019). In contrast, the phase can only be modified through time delays when using air-gun arrays. The precise control over the phase in marine vibrators facilitates the use of advanced acquisition techniques such as phase sequencing, source-side wavefield gradients, and simultaneous acquisition. Laws et al. (2019) discuss in detail the advantages of marine vibrators over conventional seismic air guns and demonstrate numerically that the aforementioned acquisition techniques can reduce acquisition time by one-third compared to conventional air gun acquisition.

The implications of a rough sea surface on seismic data are extensively studied in the literature. Laws and Kragh (2002) investigate the impact of rough sea surfaces on time-lapse experiments, showing that false structures can appear in time-lapse difference sections. Egorov et al. (2018) study the consequences of rough sea surfaces on seismic deghosting of single-component data, demonstrating that deghosting can introduce noise in the processed data. Cecconello et al. (2018) show that a time-varying sea surface introduces a Doppler shift into the recorded data. Blacquière and Sertlek (2019) and Konuk and Shragge (2020) show that rough sea surfaces scatter the ghost wavefield, introducing amplitude and phase distortions of the ghost reflections. A common element between these studies is the use of stationary sources to understand the impact of the sea surface on seismic data.

Various methods for modeling the effects of rough sea surfaces on seismic data are proposed in the literature, Kirchhoff-based methods (KMs) being the most common (e.g., Laws and Kragh, 2002; Orji et al., 2012; Egorov et al., 2018; Blacquière and Sertlek, 2019). Alternatively, Cecconello et al. (2018) exploit Rayleigh's reciprocity theorem to include ghost reflections generated from time-varying sea surfaces to ghost-free data. Konuk and Shragge (2020) model the effects of time-varying sea surfaces on the full acoustic wavefield in curvilinear coordinates using the generalized tensorial acoustic wave equation (AWE). Liu (2023) employs the chain rule to model rough sea surfaces and rough bathymetry effects in curvilinear coordinates. Robertsson et al. (2006) compare between the finite-difference method (FDM), spectral-element method (SEM), and KM for modeling the effects of rough sea surfaces on seismic data. Their work shows that FDM and SEM produce similar results, whereas KM produces results that differ from the former ones, mainly in amplitude. We refer to Konuk and Shragge (2020) for an overview of the different modeling methods to generate numerical solutions for surfaces characterized by non-Cartesian geometries.

To model marine vibrator data, Dellinger and Díaz (2020) propose splitting the sweep into different segments that can be injected at fixed source positions along the source path. JafarGandomi and Grion (2021) propose modeling marine vibrator data by interpolating unaliased impulsive sources data to desired source locations and convolving with the corresponding segments of the marine vibrator sweep. Alternatively, one can move and interpolate the source injection locations in space as a function of time to model marine vibrator sources. However, numerical instabilities and inaccuracies may arise when introducing irregular or dynamic computational geometries in Cartesian-based modeling methods, especially when implementing free-surface boundary conditions (FSBCs) for irregular geometries (de la Puente et al., 2014; Konuk and Shragge, 2020).

Accurate and stable modeling of marine vibrator data under a time-varying sea surface condition is challenging because of the complications of representing time-dependent curved surfaces in Cartesian coordinates. Approximating partial differential operators with Taylor-expansion coefficients in FDMs is the common choice when modeling seismic data because they are straightforward and easy to implement. However, accurately accounting for FS effects is difficult using such operators because they require grid points above the FS. Alternatively, one can model FS effects by using low-order accuracy coefficients (de la Puente et al., 2014) or global high-order accuracy finite-element method (FEM) (Komatitsch and Vilotte, 1998). Using FEMs places additional restrictions compared to FDMs because they require (1) time-varying meshing when considering time-varying sea surfaces, (2) meshing that conforms to all irregular internal boundaries, and (3) honoring the spatiotemporal numerical stability conditions for a time-varying mesh. Using mimetic finite-difference (MFD) operators (Castillo et al., 2001; Castillo and Miranda, 2013; de la Puente et al., 2014; Shragge and Tapley, 2017; Corbino and Castillo, 2020; Konuk and Shragge, 2020) is a viable alternative, promising a global high-order accuracy without a need for a time-dependent meshing. Thus, the MFD approach is suitable for modeling marine vibrator data in the presence of a time-varying sea surface.

In this paper, we use FDM to model the full acoustic wavefield triggered by a moving source in the presence of a time-varying sea surface. We formulate the AWE in a generalized coordinate system that effectively accounts for the source motion and time-varying free surface into the coefficients of the governing tensorial AWE. Our approach is formulated to avoid repeated velocity model interpolations or a need to interpolate the seismic wavefield below the ocean bottom to Cartesian coordinates, eliminating the added computational complexity and accuracy issues associated with this process. To test the stability of our approach, we numerically simulate marine vibrator data for an exaggerated sea state. Afterwards, we use a realistic sea state to investigate the impact of rough sea surface on marine vibrator data in the common-shot and common-receiver domains.

THEORY

Although curved surfaces can be approximated in Cartesian coordinates using smaller grid spacing, this approach results in an unjustifiable and significant increase in numerical computations, while alternative solutions that intrinsically take the non-Cartesian nature of such surfaces exist. These alternatives include methods that employ coordinate transformation within an FD framework (Carcione, 1994; Komatitsch et al., 1996; Hestholm, 1999; Hestholm and Ruud, 2002; Appelö and Petersson, 2009; de la Puente et al., 2014; Shragge, 2014; Shragge and Tapley, 2017; Konuk and Shragge, 2020), FE (Marfurt, 1984), SE (Komatitsch and Vilotte, 1998), and discontinuous Galerkin methods (Käser and Dumbser, 2006). FDMs are characterized by ease of implementation with

lower computational complexity, compared to other methods, in addition to being easily parallelizable. Thus, a natural approach is to employ a coordinate transformation that considers the intrinsic nature of moving sources and time-varying sea surfaces.

In this section, we derive a generalized 3D AWE that can model the natural response of a moving source while simultaneously accounting for a time-varying free-surface boundary due to, e.g., a complex sea state. We follow a tensorial approach to encode the geometry of these two features directly into the generalized coordinate system defined by variables $\mathbf{x}$ that we use to model the AWE response to a simulated marine vibrator source. We employ the tensorial method to transform the physical Cartesian coordinate system $\mathbf{x}$ into a static generalized coordinate system $\boldsymbol{\xi}$ that represents a uniform computational mesh. By transforming the problem in this way, we must account for the associated time- and space-varying coefficients introduced by the coordinate transformations.

1.1 Tensorial AWE

The tensorial formulation of the 3D AWE on a static computational mesh may be represented by

$$\Box_\xi P_\xi = F_\xi, \tag{1}$$

where $\Box_\xi$ is the d'Alembertian operator, subscript $\boldsymbol{\xi}$ indicates a quantity in a generalized coordinate system $\boldsymbol{\xi} = \left[\xi^0, \xi^1, \xi^2, \xi^3\right]$, P_ξ is the scalar pressure field, and F_ξ is the source term. Following Konuk and Shragge (2020) we assume that $\boldsymbol{\xi}$ is a four-vector where ξ^0 and $\left[\xi^1, \xi^2, \xi^3\right]$ respectively represent temporal and spatial coordinate variables. We further assume that ξ^1 and ξ^2 are the inline and crossline acquisition directions and that ξ^3 represents the depth axis.

Accounting for a moving source with a geometry transformation means adopting an Eulerian description centered on the moving source, which requires a mesh that accounts for its translation. We represent the geometry of the source, assumed to be moving in the ξ^1 direction with an arbitrary function $S(\xi^0, \xi^1, \xi^2, \xi^3)$ (which is independent of the crossline acquisition direction). We also assume that the sea-surface topology and associated vertical coordinate can be modeled by a generalized function $T(\xi^0, \xi^1, \xi^2, \xi^3)$. These specifications allow us to write a generalized transformation connecting the physical generalized observation coordinates $\mathbf{x}$ with the static computational coordinates $\boldsymbol{\xi}$ according to

$$\begin{bmatrix} x^0 \\ x^1 \\ x^2 \\ x^3 \end{bmatrix} = \begin{bmatrix} i\xi^0 \\ S(\xi^0, \xi^1, \xi^2, \xi^3) \\ \xi^2 \\ T(\xi^0, \xi^1, \xi^2, \xi^3) \end{bmatrix}, \tag{2}$$

where the introduction of the imaginary unit i is explained below.

Using the unique mapping between the $\boldsymbol{\xi}$- and $\mathbf{x}$-coordinate systems, we define the corresponding covariant metric tensor $g_{\mu\nu}$, which is a symmetric 4×4 matrix that captures the spatially and temporally varying geometry (i.e., how the mesh compresses, rarefies, and shears as a function of space and time) of this 4D coordinate transformation, such that

$$g_{\mu\nu} = \frac{\partial x^\alpha}{\partial \xi^\mu} \frac{\partial x^\alpha}{\partial \xi^\nu}, \quad \alpha, \mu, \nu = 0, 1, 2, 3. \tag{3}$$

The introduction of the imaginary unit i follows the Minkowski space definition, which combines time (imaginary axis) and the 3D Euclidean space (real axes) into a 4D manifold. An immediate consequence of Minkowski space definition is that seismic events are causally connected (e.g., seismic waves reflect when an incident wavefield interacts with reflectors).

The tensorial AWE requires a contravariant representation of the metric tensor $g^{\mu\nu}$ (Shragge, 2014), which may be calculated as a point-wise matrix inverse of the covariant metric tensor $g_{\mu\nu}$. Using the general form of 4D coordinate mapping given in equation 2 results in the following analytic metric tensor inverse:

$$g^{\mu\nu} = \begin{bmatrix} -1 & g^{01} & 0 & g^{03} \\ g^{01} & g^{11} & g^{12} & g^{13} \\ 0 & g^{12} & 1 & g^{23} \\ g^{03} & g^{13} & g^{23} & g^{33} \end{bmatrix} \tag{4}$$

$$= \begin{bmatrix} -1 & \frac{a_{03}}{a_{13}} & 0 & -\frac{a_{01}}{a_{13}} \\ \frac{a_{03}}{a_{13}} & \frac{a_{23}{}^2 - a_{03}{}^2 + S_3{}^2 + T_3{}^2}{a_{13}{}^2} & -\frac{a_{23}}{a_{13}} & \frac{a_{01}a_{03} - a_{21}a_{23} - S_1S_3 - T_1T_3}{a_{13}{}^2} \\ 0 & -\frac{a_{23}}{a_{13}} & 1 & -\frac{a_{12}}{a_{13}} \\ -\frac{a_{01}}{a_{13}} & \frac{a_{01}a_{03} - a_{21}a_{23} - S_1S_3 - T_1T_3}{a_{13}{}^2} & -\frac{a_{12}}{a_{13}} & \frac{a_{21}{}^2 - a_{01}{}^2 + S_1{}^2 + T_1{}^2}{a_{13}{}^2} \end{bmatrix}, \tag{5}$$

where $S_i \equiv \frac{\partial S}{\partial \xi^i}$, $T_i \equiv \frac{\partial S}{\partial \xi^i}$, and $a_{ij} \equiv S_i T_j - T_i S_j$. In addition, the square root of the covariant metric tensor determinant is $\sqrt{|g|} = |a_{13}|$, which is required in the tensorial AWE formulation.

1.2   Coupled first-order acoustic PDE system

The dynamics of the first-order coupled acoustic PDE system are governed by two operators. The first is the generalized gradient operator $\mathcal{G}^\mu$ that acts on a rank-zero tensor field U

$$\mathcal{G}^\mu[U] = g^{\mu\nu} \frac{\partial U}{\partial \xi^\nu}. \tag{6}$$

The second is the generalized divergence operator $\mathcal{D}_\mu$ that acts on a tensor object χ^ν

$$\mathcal{D}_\mu[\chi^\nu] = \frac{1}{\sqrt{|g|}} \frac{\partial}{\partial \xi^\mu} \left(\sqrt{|g|} \chi^\nu \right). \tag{7}$$

The acoustic operator in equation 1 can be written as

$$\Box_\xi = -\mathcal{D}_\mu \mathcal{G}^\mu P_\xi = F_\xi \tag{8}$$

or equivalently as (Konuk and Shragge, 2020)

$$-\frac{1}{\sqrt{|g|}} \frac{\partial}{\partial \xi^\mu} \left(\sqrt{|g|} g^{\mu\nu} \frac{\partial}{\partial \xi^\nu} \right) P_\xi = F_\xi. \tag{9}$$

Using these operators, the coupled first-order acoustic PDE system can be written as the generalized linearized continuity equation (LCE):

$$-\mathcal{G}^0[P_\xi] = \mathcal{D}_i[u_\xi^i] + F_\xi, \tag{10}$$

and the vector generalized linearized Euler equation (LEE) (i.e., Newtonian force):

$$\mathcal{D}_0\left[u_\xi^i\right] = \mathcal{G}^i[P_\xi], \tag{11}$$

where $i = 1, 2, 3$ is an index over the spatial variable coordinates. Thus, we may rewrite the LCE in equation 10 as

$$-g^{0\nu} \frac{\partial P_\xi}{\partial \xi^\nu} = \frac{1}{\sqrt{|g|}} \frac{\partial}{\partial \xi^i} \left(\sqrt{|g|} u^i \right) + F_\xi, \tag{12}$$

and the vector LEE in equation 11 as

$$\frac{1}{\sqrt{|g|}} \frac{\partial}{\partial \xi^0} \left(\sqrt{|g|} u_\xi^i \right) = g^{i\nu} \frac{\partial P_\xi}{\partial \xi^\nu}. \tag{13}$$

1.3   3D Moving source with time-varying sea surface

We can now write the equations when including the moving source, assumed to be moving laterally in the ξ^1 direction, and a time-varying sea surface. The specific LCE equation for this is given by:

$$\frac{\partial P_\xi}{\partial \xi^0} - g^{01} \frac{\partial P_\xi}{\partial \xi^1} - g^{03} \frac{\partial P_\xi}{\partial \xi^3} = \frac{1}{\sqrt{|g|}} \left[\frac{\partial}{\partial \xi^1} \left(\sqrt{|g|} u^1 \right) + \frac{\partial}{\partial \xi^2} \left(\sqrt{|g|} u^2 \right) + \frac{\partial}{\partial \xi^3} \left(\sqrt{|g|} u^3 \right) \right] + F_\xi, \tag{14}$$

which using $\frac{\partial}{\partial \xi^0} \equiv \frac{1}{c_\xi} \frac{\partial}{\partial \tau}$ can be rewritten

$$\frac{1}{c_\xi} \frac{\partial P_\xi}{\partial \tau} - \frac{a_{03}}{a_{13}} \frac{\partial P_\xi}{\partial \xi^1} - \frac{a_{01}}{a_{31}} \frac{\partial P_\xi}{\partial \xi^3} = \frac{1}{a_{13}^*} \left[\frac{\partial}{\partial \xi^1} \left(a_{13}^* u^1 \right) + \frac{\partial}{\partial \xi^2} \left(a_{13}^* u^2 \right) + \frac{\partial}{\partial \xi^3} \left(a_{13}^* u^3 \right) \right] + F_\xi, \tag{15}$$

where $a_{13}^* \equiv |a_{13}|$. Similarly, the vector LEE equation can be rewritten as

$$\frac{1}{c_\xi a_{13}^*} \frac{\partial}{\partial \tau} \left(a_{13}^* u_\xi^1 \right) = \frac{g^{01}}{c_\xi} \frac{\partial P_\xi}{\partial \tau} + g^{11} \frac{\partial P_\xi}{\partial \xi^1} + g^{12} \frac{\partial P_\xi}{\partial \xi^2} + g^{13} \frac{\partial P_\xi}{\partial \xi^3}, \tag{16}$$

$$\frac{1}{c_\xi a_{13}^*} \frac{\partial}{\partial \tau} \left(a_{13}^* u_\xi^2 \right) = g^{12} \frac{\partial P_\xi}{\partial \xi^1} + \frac{\partial P_\xi}{\partial \xi^2} + g^{23} \frac{\partial P_\xi}{\partial \xi^3}, \tag{17}$$

$$\frac{1}{c_\xi a_{13}^*} \frac{\partial}{\partial \tau} \left(a_{13}^* u_\xi^3 \right) = \frac{g^{03}}{c_\xi} \frac{\partial P_\xi}{\partial \tau} + g^{13} \frac{\partial P_\xi}{\partial \xi^1} + g^{23} \frac{\partial P_\xi}{\partial \xi^2} + g^{33} \frac{\partial P_\xi}{\partial \xi^3}. \tag{18}$$
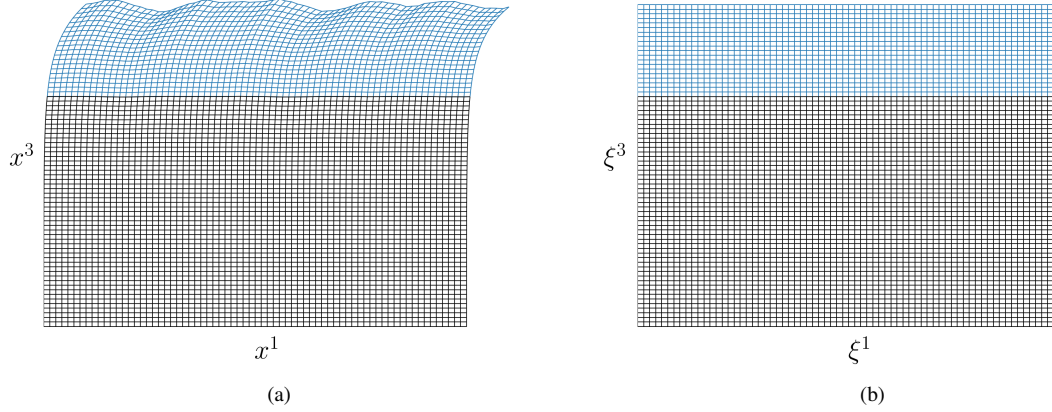
Figure 1. Graphical representation of (a) physical and (b) computational domains.

1.4 Coordinate transformation

To facilitate the developed theory in modeling a moving source in the presence of a time-varying sea surface, we make a set of plausible assumptions: (1) no stretching of the time axis; (2) the source moves along the ξ^1-axis; (3) the source moves at a fixed depth level; (4) the source moves at a constant velocity; and (5) the source moves in a homogeneous fluid medium. Assumptions (3) and (5) allow us to define a coordinate transformation that confines the physical mesh deformation to the assumed homogeneous fluid medium. Given the set of assumptions, we can define a depth-dependent coordinate transformation that tracks the source movement such that

$$S(\xi^0, \xi^1, \xi^2 = x^2, \xi^3) = \xi^1 + v\xi^0 e^{\gamma(z_s - \xi^3)}, \tag{19}$$

and a depth-dependent coordinate transformation that accounts for the time-varying sea surface such that

$$T(\xi^0, \xi^1, \xi^2, \xi^3) = \xi^3 + W\left(\xi^1, \xi^2, \tau\right)\left(1 - \frac{\xi^3}{\xi_m^3}\right)e^{\lambda\xi^3}, \tag{20}$$

where v is the vessel velocity, z_s is the source depth, W is the time-varying sea-surface function, $\xi_m^3 = x_m^3$ is the maximum model depth, and γ and λ are user-defined decay factors that control the amount of horizontal and vertical deformations as a function of depth, respectively. A judicious choice of γ and λ confines the mesh deformation to the homogeneous water layer, mitigating the need for a repeated and expensive interpolation of subsurface physical properties (i.e., $c_\xi = c_x$) and seismic wavefield associated with time-varying meshes below the ocean bottom. To compute $\frac{\partial T}{\partial \xi^0}$, as required for the metric tensor, we use $\frac{\partial \tau}{\partial \xi^0} = \frac{1}{c_\xi}$ such that

$$\frac{\partial T}{\partial \xi^0} = \frac{1}{c_\xi}\frac{\partial W}{\partial \tau}\left(1 - \frac{\xi^3}{\xi_m^3}\right)e^{\lambda\xi^3}. \tag{21}$$

Figure 1(a) and 1(b) shows graphical representations of a deformed physical domain in Cartesian coordinates and the fixed computational domain in a generalized coordinate system, respectively.

1.5 Time-varying sea surface

We use a modified Pierson and Moskowitz (1964) power spectrum that includes a directivity term to model time-varying sea surfaces (Laws and Kragh, 2002). The modified power spectrum is defined as

$$\tilde{W}(k_x, k_z, \tau) = \frac{\alpha N}{2k^4}\exp\left(\frac{-\beta^2 G^2}{k^2 U^4}\right)\cos^{2s}\left(\frac{\theta}{2}\right) + G\left(k_x, k_z, \tau\right), \tag{22}$$

where $\alpha = 0.0081$ and $\beta = 0.74$ are dimensionless constants; N is a normalization factor, such that $\int N\cos^{2s}\left(\frac{\theta}{2}\right)d\theta = 1$; $k = \sqrt{k_x^2 + k_z^2}$ is the wavenumber in radians per meter; G is the gravitational acceleration constant; U is the wind speed measured at 19 m above the sea surface; θ is azimuthal angle relative to the wind direction; s is an empirical spreading factor; and G is a time-varying random Gaussian number to model a 2D time-varying sea surface.

Numerical approach

The goal of this section is to provide a practical approach to numerically solve the 2D coupled first-order system. We use a fully-staggered grid (FSG) scheme with MFD operators to ensure numerical stability and accuracy when solving the tensorial AWE in generalized coordinates. We also use a prediction step staggered-in-time (PSIT) scheme to compute the fluid advection terms in the LCE equation.

1.6   Fully staggered grid

Modeling wave propagation in Cartesian coordinates using a first-order coupled system allows using a standard staggered grid (SSG) scheme (Figure 2(a)), improving the overall accuracy and stability of the numerical solution (e.g., Virieux, 1986). Furthermore, implementing robust absorbing boundary conditions, e.g., perfectly matched layers, is more straightforward in first-order systems than in second-order formulations of the AWE. However, facilitating Cartesian-to-generalized coordinate transformation to model a moving source with a time-varying sea surface introduces mixed derivatives and advection terms into the governing tensorial AWE; otherwise, these terms would vanish in standard Cartesian-based implementations characterized by flat surfaces. Solving the generalized first-order system requires evaluating mixed partial derivatives at locations where the seismic wavefield is not readily available when using an SSG scheme. One solution is to use a high-order interpolation of the wavefield for all time steps, which is computationally expensive and inefficient. A more natural choice is to use a fully staggered grid (FSG) scheme with complementary grid locations (Lisitsa and Vishnevskiy, 2010) that provides all the required wavefield samples, constructed using a coupled SSG schemes set spatially with a diagonal offset (Figure 2(b)).

1.7   Mimetic finite-difference operators

Approximating partial differential operators using Taylor-based coefficients is appealing for their simplicity and ease of implementation when solving the AWE. A drawback of such operators is the reduced order of accuracy at the boundaries of the modeling domain, which can introduce numerical instability when modeling free-surface effects of curved surfaces, much less when considering time-varying free surfaces. Alternatively, MFD operators provide a uniform order of accuracy throughout the modeling domain, including the boundary region (Castillo and Miranda, 2013; de la Puente et al., 2014; Shragge and Tapley, 2017; Konuk and Shragge, 2020). These operators are analogs to their continuum gradient and divergence counterparts that mimic the mathematical and physical relations that govern the seismic wavefield and satisfy fundamental properties such as conservation laws, symmetry, and duality of differential operators (Lipnikov et al., 2014).

   To facilitate MFD operators within the boundary region, additional complementary pressure and particle velocity overlapping grid points are required (Figure 2(c)). Corbino and Castillo (2020) formulate the numerical gradient ($\mathbf{G}$) and divergence ($\mathbf{D}$) operators. These operators have different coefficients within the boundary region than Taylor-based coefficients, but similar coefficients away from the boundary region. We differentiate between fields defined on full-integer ($\mathbf{f}$) and half-integer ($\mathbf{h}$) grids. It is important to note that the numerical operators are defined based on the grid layout within the numerical scheme (i.e., the numerical gradient ($\mathbf{G}$) and divergence ($\mathbf{D}$) operators are applied on fields defined on half- and full-integer grids, respectively).

   In the 2D MFD formulation, the pressure field is defined at $[\xi^1, \xi^3] = [\mathbf{f}, \mathbf{f}]$ and $[\xi^1, \xi^3] = [\mathbf{h}, \mathbf{h}]$, which we denote by $P_\xi[\mathbf{f}, \mathbf{f}]$ (Figure 3(a)) and $P_\xi[\mathbf{h}, \mathbf{h}]$ (Figure 3(b)), respectively; whereas the particle velocity field is defined at $[\xi^1, \xi^3] = [\mathbf{f}, \mathbf{h}]$ and $[\xi^1, \xi^3] = [\mathbf{h}, \mathbf{f}]$, which we denote by $U_\xi[\mathbf{f}, \mathbf{h}]$ (Figure 3(c)) and $U_\xi[\mathbf{h}, \mathbf{f}]$ (Figure 3(d)), respectively. To approximate $\mathcal{D}_i[u_\xi^i]$ and $\mathcal{G}^i[P_\xi]$, we apply the numerical operators as shown in Table 1.

1.8   Prediction step staggered-in-time

The advection terms in the LCE equation present us with two implementation challenges: (1) the partial derivatives are not centered at required pressure grid points; and (2) they are required to be at half-integer time steps when using a leap-frog scheme. In an SSG scheme, the pressure and particle velocity wavefields are usually advanced using a leap-frog scheme for its practical memory requirement. One can use an unstaggered-in-time approach when advancing the pressure and particle velocity wavefields to solve the time-stepping problem. However, an unstaggered-in-time approach requires storing wavefields at different time steps, doubling memory requirement (Konuk and Shragge, 2020). An alternative approach is to implement a prediction step staggered-in-time (PSIT) scheme while (reasonably) assuming the mesh moves much slower than the wave propagation speed. In the PSIT scheme, we advance the pressure wavefield for full- and half-time steps, neglecting the advection terms in equation **??**. Then, we compute
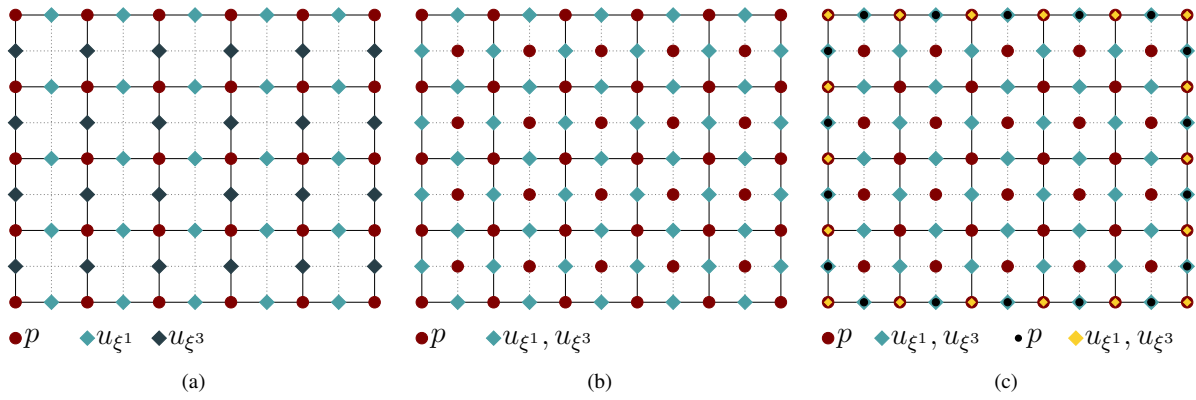
Figure 2. Graphical representation of (a) SSG, (b) FSG, and (c) MFD staggered grid computational domains.
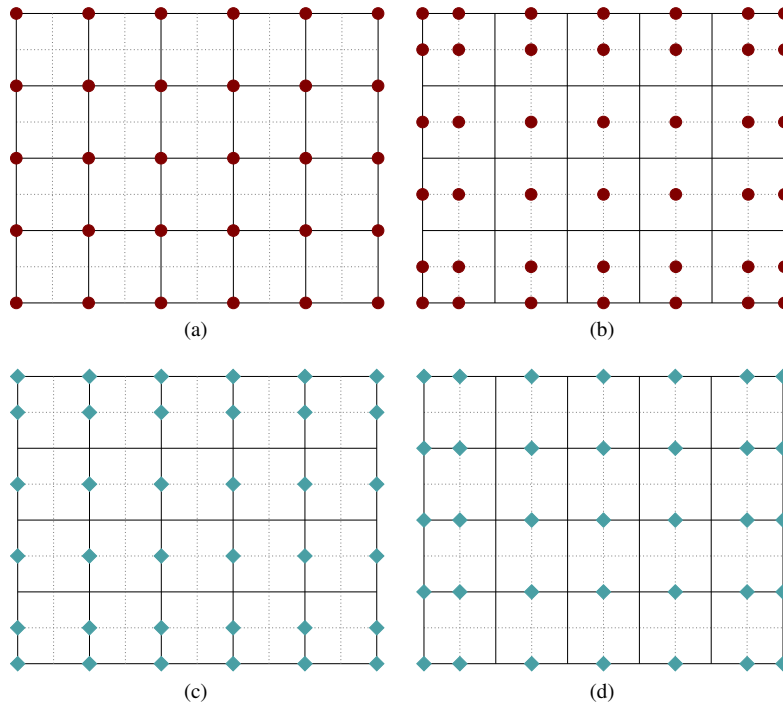

Figure 3. Graphical representation of pressure field defined at (a) $[\xi^1, \xi^3] = [\mathbf{f}, \mathbf{f}]$ and (b) $[\xi^1, \xi^3] = [\mathbf{h}, \mathbf{h}]$ grid points, and particle velocity field defined at (c) $[\xi^1, \xi^3] = [\mathbf{f}, \mathbf{h}]$ and (d) $[\xi^1, \xi^3] = [\mathbf{h}, \mathbf{f}]$ grid points.

and add the spatial derivatives of the pressure wavefield at the half-time step to the pressure wavefield at the full-time step. Because

Table 1. Differential operators as applied to the pressure and particle velocity fields within an MFD scheme.

Differential operator	Numerical operator	To update
$\mathcal{D}_1\left[u_\xi^1[\mathbf{h},\mathbf{f}]\right]$	$\mathbf{G}^1 u_\xi^1[\mathbf{h},\mathbf{f}]$	$P_\xi[\mathbf{f},\mathbf{f}]$
$\mathcal{D}_3\left[u_\xi^3[\mathbf{f},\mathbf{h}]\right]$	$\mathbf{G}^3 u_\xi^3[\mathbf{f},\mathbf{h}]$	$P_\xi[\mathbf{f},\mathbf{f}]$
$\mathcal{D}_1\left[u_\xi^1[\mathbf{f},\mathbf{h}]\right]$	$\mathbf{D}_1 u_\xi^1[\mathbf{f},\mathbf{h}]$	$P_\xi[\mathbf{h},\mathbf{h}]$
$\mathcal{D}_3\left[u_\xi^3[\mathbf{h},\mathbf{f}]\right]$	$\mathbf{D}_3 u_\xi^3[\mathbf{h},\mathbf{f}]$	$P_\xi[\mathbf{h},\mathbf{h}]$
$\mathcal{G}^1\left[P_\xi[\mathbf{h},\mathbf{h}]\right]$	$\mathbf{G}^1 P_\xi[\mathbf{h},\mathbf{h}]$	$u_\xi^i[\mathbf{f},\mathbf{h}]$
$\mathcal{G}^3\left[P_\xi[\mathbf{f},\mathbf{f}]\right]$	$\mathbf{D}_3 P_\xi[\mathbf{f},\mathbf{f}]$	$u_\xi^i[\mathbf{f},\mathbf{h}]$
$\mathcal{G}^1\left[P_\xi[\mathbf{f},\mathbf{f}]\right]$	$\mathbf{D}_1 P_\xi[\mathbf{f},\mathbf{f}]$	$u_\xi^i[\mathbf{h},\mathbf{f}]$
$\mathcal{G}^3\left[P_\xi[\mathbf{h},\mathbf{h}]\right]$	$\mathbf{G}^3 P_\xi[\mathbf{h},\mathbf{h}]$	$u_\xi^i[\mathbf{h},\mathbf{f}]$

the advection terms must be centered at pressure grid points, we approximate them using Taylor-based coefficients given by

$$\frac{1}{840}\begin{bmatrix}
-1750 & 3360 & -2520 & 1120 & -210 & 0 & \cdots & \cdots & \cdots \\
-210 & -700 & 1260 & -420 & 70 & 0 & \cdots & \cdots & \cdots \\
70 & -560 & 0 & 560 & -70 & 0 & \cdots & \cdots & \cdots \\
0 & 70 & -560 & 0 & 560 & -70 & 0 & \cdots & \cdots \\
\vdots & \ddots & \ddots & \ddots & \ddots & \ddots & \ddots & \ddots & \vdots \\
\cdots & \cdots & 0 & 70 & -560 & 0 & 560 & -70 & 0 \\
\cdots & \cdots & \cdots & 0 & 70 & -560 & 0 & 560 & -70 \\
\cdots & \cdots & \cdots & 0 & -70 & 420 & -1260 & 700 & 210 \\
\cdots & \cdots & \cdots & 0 & 210 & -1120 & 2520 & -3360 & 1750
\end{bmatrix}$$

and

$$\frac{1}{840}\begin{bmatrix}
-2816 & 3675 & -1225 & 441 & -75 & 0 & \cdots & \cdots & \cdots \\
-768 & 140 & 840 & -252 & 40 & 0 & \cdots & \cdots & \cdots \\
256 & -840 & 140 & 504 & -60 & 0 & \cdots & \cdots & \cdots \\
0 & 70 & -560 & 0 & 560 & -70 & 0 & \cdots & \cdots \\
\vdots & \ddots & \ddots & \ddots & \ddots & \ddots & \ddots & \ddots & \vdots \\
\cdots & \cdots & 0 & 70 & -560 & 0 & 560 & -70 & 0 \\
\cdots & \cdots & \cdots & 0 & 60 & -504 & -140 & 840 & -256 \\
\cdots & \cdots & \cdots & 0 & -40 & 252 & -840 & -140 & 768 \\
\cdots & \cdots & \cdots & 0 & 75 & -441 & 1225 & -3675 & 2816
\end{bmatrix}$$

to update the pressure wavefield at full-integer ($P_\xi[\mathbf{f},\mathbf{f}]$) and half-integer ($P_\xi[\mathbf{h},\mathbf{h}]$) grids, respectively.

Numerical Examples

This section demonstrates the effects of time-varying sea surfaces on marine vibrator data in the common-shot and common-receiver domains. In the first example, we use an unrealistically exaggerated sea state with a significant wave height (SWH) of ±14 m with an apparent lateral velocity of 175 m/s to (1) validate the stability of the numerical scheme and (2) emphasize the effects of a time-varying sea surface on seismic data. In the second example, we use a more realistic SWH of ±5 m with the same apparent lateral velocity as in the first example to highlight the significance of time-varying sea surfaces on seismic data in the common-receiver domain.

1.9   Exaggerated sea state

In this example, we simulate the acoustic wavefield using a Marmousi II sub-model (Martin et al., 2002), resampled such that $dx = dz = 1.5$ m. We use a source placed at $[\xi^1, \xi^3] = [900, 30]$ m that moves at 5 m/s, and 1201 stationary receivers positioned at $\xi^3 = x^3 = 250$ m with a 1.5 m uniform spacing. The source function is a linear sweep from 20 to 60 Hz of 0.5 s duration.

Figure 4(a) and 4(b) shows snapshots of the seismic wavefield triggered by a moving source assuming flat and rough sea surfaces, respectively. The time-varying sea-surface scenario is characterized by amplitude and phase distortions because of the scattering effects on the wavefield introduced by the rough sea surface, whereas the flat sea surface case exhibits a simpler radiation pattern for ghost reflections. We note that the source-side ghost reflections are easily visible because of the significant source depth and long duration of the sweep.

Figure 5(a) and 5(b) shows the corresponding shot gathers of the two simulations, respectively. The ghost reflections in the time-varying sea-surface shot gather exhibit amplitude and phase distortions, making them less predictable compared to the flat sea-surface shot gather scenario (Figure 6). Because the wavefield interacts with a time-varying sea surface, the ghost reflections vary in space and time. Further, the ghost notches are dispersed and blurred. To see the profound effects of a time-varying sea surface on reflection data, we repeat the numerical simulations for a stationary source, keeping all other parameters unchanged. Figure 7(a) and 7(b) shows a time-windowed shot gathers after correlating with the stationary sweep. We can see that the continuity and amplitude of the seismic events are severely affected when the wavefield interacts with a time-varying sea surface. Such effects make data processing challenging and reduce the repeatability of seismic data.

1.10   Realistic sea state

In this example, we investigate the impact of time-varying sea surfaces on seismic data in the common-receiver domain, especially since ocean-bottom data are commonly processed in such a domain because of the sparse receiver sampling. We use the same modeling parameters as in the previous example, but model 301 sources with a 6 m source spacing. Figure 8(a) and 8(b) shows shot gathers simulated with a flat and time-varying sea surface, respectively. Under a realistic sea state acquisition condition, the effects of a time-varying sea surface, although present, are hardly visible because of the long duration of the sweep; the ghost wavefield is scattered and dispersed, thus easily masked by the wavefield generated by later parts of the sweep. In fact, the two gathers are indistinguishable, making an inference about the sea state from shot gathers challenging. Figure 8(c) and 8(d) shows common-receiver gathers simulated with a flat and time-varying sea surface, respectively. In the common-receiver domain, the effects of time-varying sea surfaces are easily noticeable because different traces are simulated with different source positions and time-varying sea surfaces, creating trace-to-trace jitter as reported by Blacquière and Sertlek (2019). Typical marine sources use a buoy to control their depth during acquisition (Laws and Kragh, 2002); accordingly, the depth of a marine source is measured relative to the sea surface directly above the source. Thus, the incident wavefield that has not interacted with the sea surface is also affected by the time-varying sea surface because of the variable source depth (we inherently account for the variable source depth due to the rough sea surface in our coordinate transformation). Therefore, the variable source depth also creates a trace-to-trace jitter in the common-receiver domain. In a shot gather, however, the effect of a variable-depth source manifests as time-dependent frequency shifts (i.e., Doppler effect) for long sweeps.

Discussion

The time-varying nature of the sea surface poses a processing challenge, especially for time-lapse studies, because false structures can appear in time-lapse difference sections even for fairly calm sea states (Laws and Kragh, 2002). Further repeatability challenges arise when considering moving and long-emitting sources, such as source/receiver positioning and the interaction of long sweeps with the time-varying sea surface. Accurately accounting for source motion and time-varying sea surface in modeling is essential to understand the effects of realistic acquisition conditions on seismic data. More importantly, modeling such effects provides an opportunity to validate processing workflows for time-lapse data.

Modeling marine vibrator data in the presence of a time-varying sea surface requires using an MFD approach to ensure accuracy and numerical stability when the seismic wavefield interacts with the time-varying free surface. MFD operators, as opposed to Taylor-based coefficients, provide a uniform high-order accuracy throughout the modeling domain. Inaccurate implementation of the FSBC introduces numerical artifacts, making the numerical scheme unstable (Konuk and Shragge, 2020). Additionally, using an MFD scheme provides required wavefield samples to compute cross-derivative terms; otherwise, it would require expensive high-order wavefield interpolation when using an SSG scheme.

Modeling the time-dependent tensorial AWE in a generalized coordinate system requires repeated interpolation of the subsurface physical properties (defined in Cartesian coordinates) to conform to the time-varying mesh grid. To preclude that requirement, we introduce depth-dependent decaying factors to confine the mesh deformation to the homogeneous water layer, making the two coordinate systems identical below the ocean-bottom level. An advantage of such an approach is that the wavefield can be sampled at and below the receivers level without a need to interpolate it back to Cartesian coordinates.
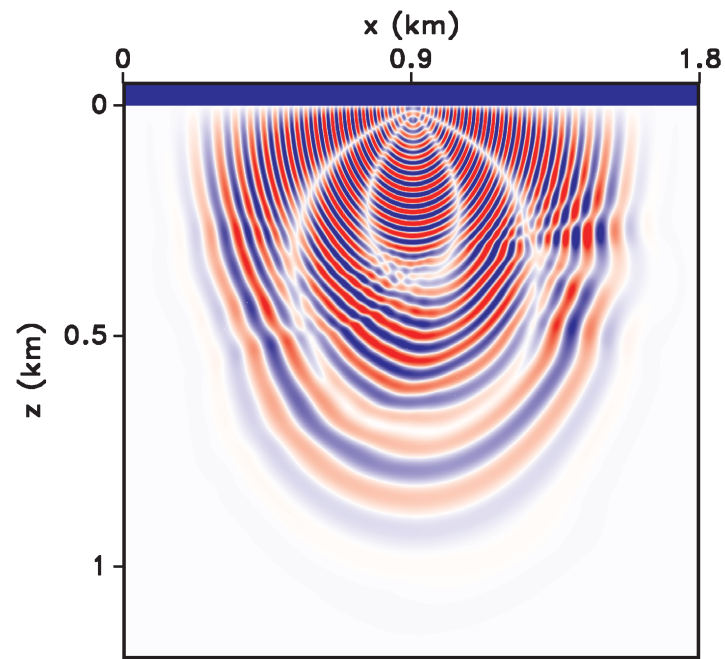
(a)
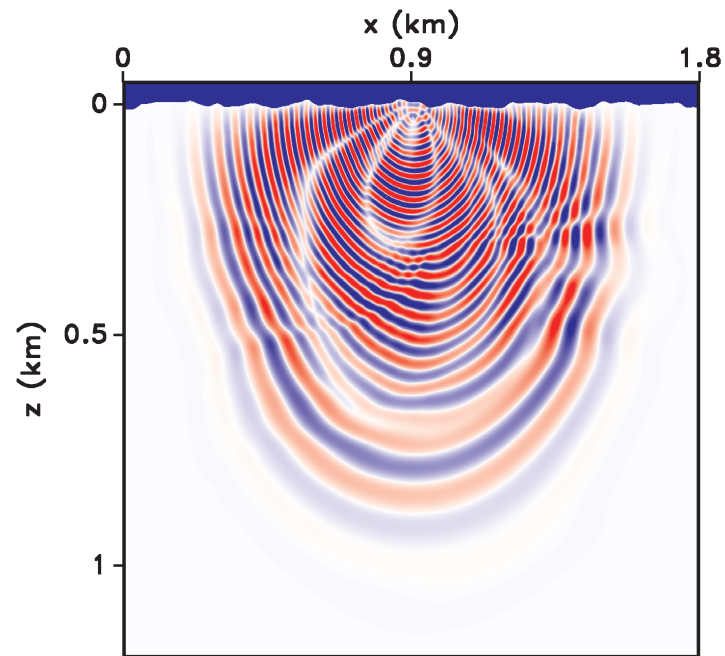
(b)

Figure 4. Wavefield snapshots simulated using (a) flat and (b) rough sea surface with ±14 m SWH. The time-varying sea surface scenario is characterized by amplitude and phase distortions because of the scattering effects on the wavefield introduced by the rough sea surface.
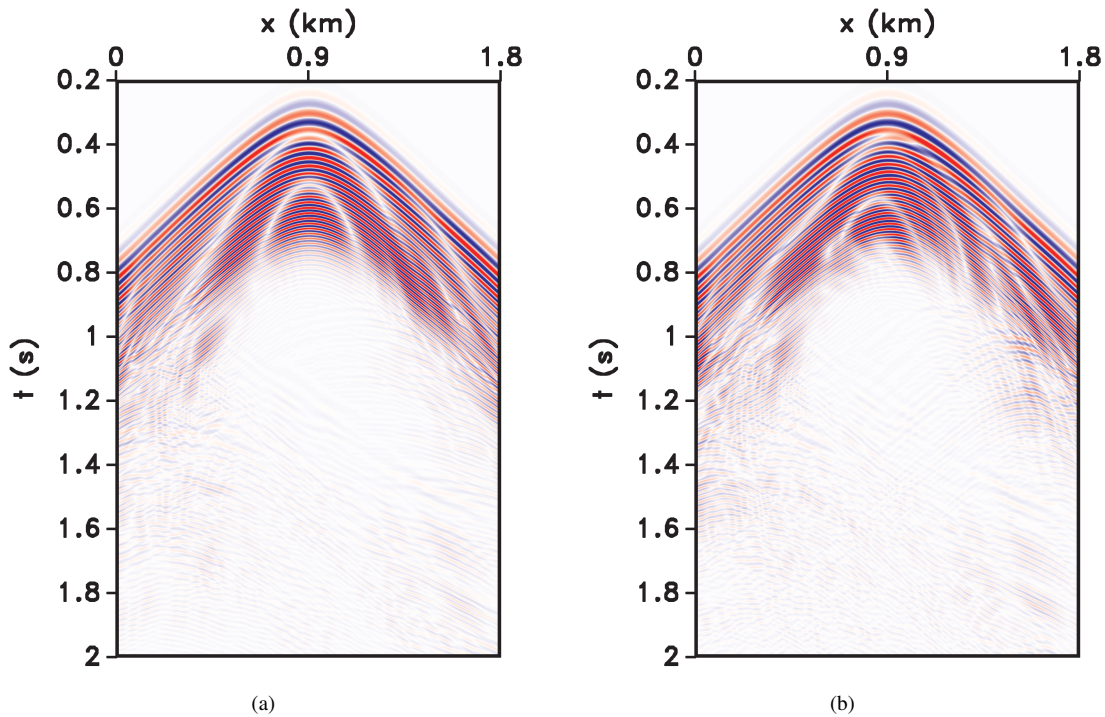
Figure 5. Shot gathers for (a) flat and (b) rough sea surface with ± 14 m SWH. The flat sea surface shot gather is characterized by a simple ghost-reflection interference pattern, whereas a more complex interference pattern characterizes the rough sea surface shot gather.

2 CONCLUSIONS

We present a finite-difference approach to model the full acoustic wavefield triggered by a moving source in the presence of a time-varying sea surface. The developed approach employs a time-dependent coordinate transformation to solve the tensorial acoustic wave equation on a uniformly spaced and time-invariant computational domain. Although we assume the source moves at a constant velocity and depth level, incorporating a variable source velocity and depth is straightforward. This work is not limited to modeling marine vibrator data, but can also model towed-streamer data.

In the numerical examples, we show that for an exaggerated sea state, the effects of a time-varying sea surface are clearly visible in the shot domain. For realistic sea states, inferring the different states (e.g., from being flat to being rough) in this domain is hard; however, the effects of a realistic time-varying sea surface are visible in the common-receiver domain. The sea-surface effects can have consequences on seismic data processing and imaging, and on subsequent seismic data interpretation and attribute analyses. The developed approach provides a tool to validate marine vibrator data processing and understand the consequences of a moving source and time-varying sea surface on seismic imaging and inversion.
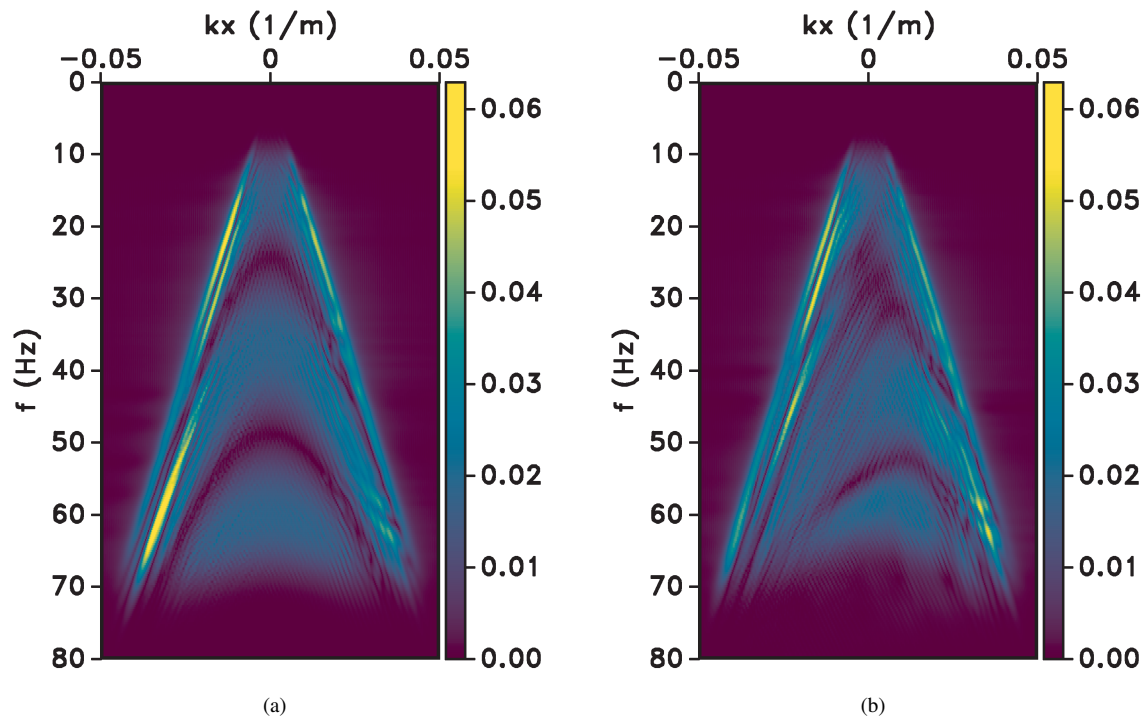
3 ACKNOWLEDGMENTS

Figure 6. Frequency-wavenumber spectra of shot gathers shown in (a) Figure 5(a) and (b) Figure 5(b). The ghost notches are predictable in the FK spectrum of the flat sea-surface shot gather, whereas they are dispersed and blurred in the FK spectrum of the rough sea-surface shot gather.

REFERENCES

Appelö, D., and N. A. Petersson, 2009, A stable finite difference method for the elastic wave equation on complex geometries with free surfaces: Communications in Computational Physics, **5**, no. 1, 84–107.

Blacquière, G., and H. O. Sertlek, 2019, Modeling and assessing the effects of the sea surface, from being flat to being rough and dynamic: Geophysics, **84**, no. 2, T13–T27, doi:10.1190/geo2018-0294.1.

Carcione, J. M., 1994, The wave equation in generalized coordinates: Geophysics, **59**, no. 12, 1911–1919, doi:10.1190/1.1443578.

Castillo, J. E., J. M. Hyman, M. Shashkov, and S. Steinberg, 2001, Fourth-and sixth-order conservative finite difference approximations of the divergence and gradient: Applied Numerical Mathematics, **37**, no. 1, 171–187, doi:10.1016/S0168-9274(00)00033-7.

Castillo, J. E., and G. F. Miranda, 2013, Mimetic discretization methods: CRC Press.

Cecconello, E., E. G. Asgedom, O. C. Orji, M. W. Pedersen, and W. Söllner, 2018, Modeling scattering effects from time-varying sea surface based on acoustic reciprocity: Geophysics, **83**, no. 2, T49–T68, doi:10.1190/geo2017-0410.1.

Corbino, J., and J. E. Castillo, 2020, High-order mimetic finite-difference operators satisfying the extended Gauss divergence theorem: Journal of Computational and Applied Mathematics, **364**, 112326, doi:10.1016/j.cam.2019.06.042.

de la Puente, J., M. Ferrer, M. Hanzich, J. E. Castillo, and J. M. Cela, 2014, Mimetic seismic wave modeling including topography on deformed staggered grids: Geophysics, **79**, no. 3, T125–T141, doi:10.1190/geo2013-0371.1.

Dellinger, J., and E. Díaz, 2020, Efficient modelling of extended-duration moving seismic sources: EAGE 2020 annual conference & exhibition online, 1–5, doi:10.3997/2214-4609.202010838.

Dellinger, J., A. Ross, D. Meaux, A. Brenders, G. Gesoff, J. Etgen, J. Naranjo, G. Openshaw, and M. Harper, 2016, Wolfspar®, an "FWI-friendly" ultra-low-frequency marine seismic source: 86th Annual International Meeting, SEG, Expanded Abstracts, 4891–4895, doi:10.1190/segam2016-13762702.1.

Dragoset, W. H., 1988, Marine vibrators and the Doppler effect: Geophysics, **53**, no. 11, 1388–1398, doi:10.1190/1.1442418.

Egorov, A., S. Glubokovskikh, A. Bóna, R. Pevzner, B. Gurevich, and M. Tokarev, 2018, How rough sea affects marine seismic data and deghosting procedures: Geophysical Prospecting, **66**, no. 1, 3–12, doi:10.1111/1365-2478.12535.

Fomel, S., P. Sava, I. Vlad, Y. Liu, and V. Bashkardin, 2013, Madagascar: Open-source software project for multidimensional data analysis and reproducible computational experiments: Journal of Open Research Software, **1**, no. 1, doi:10.5334/jors.ag.
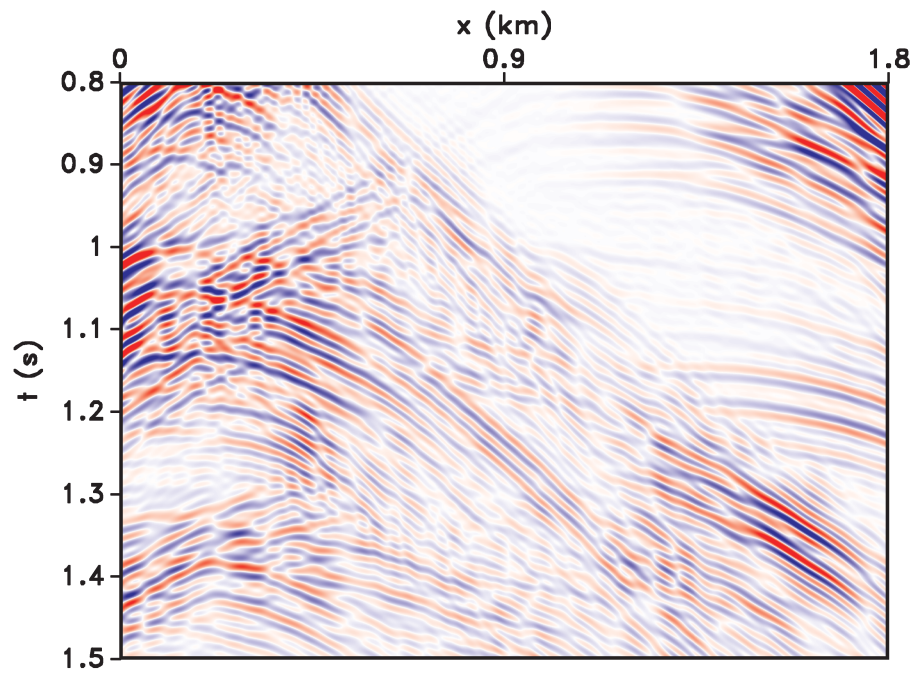
(a)
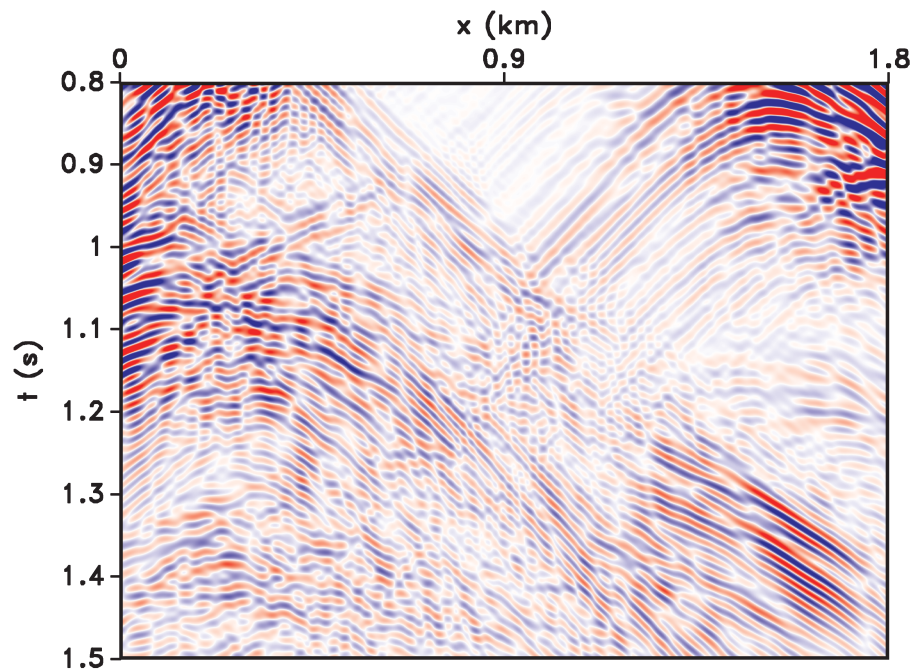
(b)

Figure 7. Time-window of correlated shot gathers simulated using a stationary source with (a) flat and (b) rough sea surface with ±14 m SWH. The continuity and amplitude of seismic events are severely affected when the wavefield interacts with a time-varying sea surface compared to when the wavefield interacts with a flat sea surface.
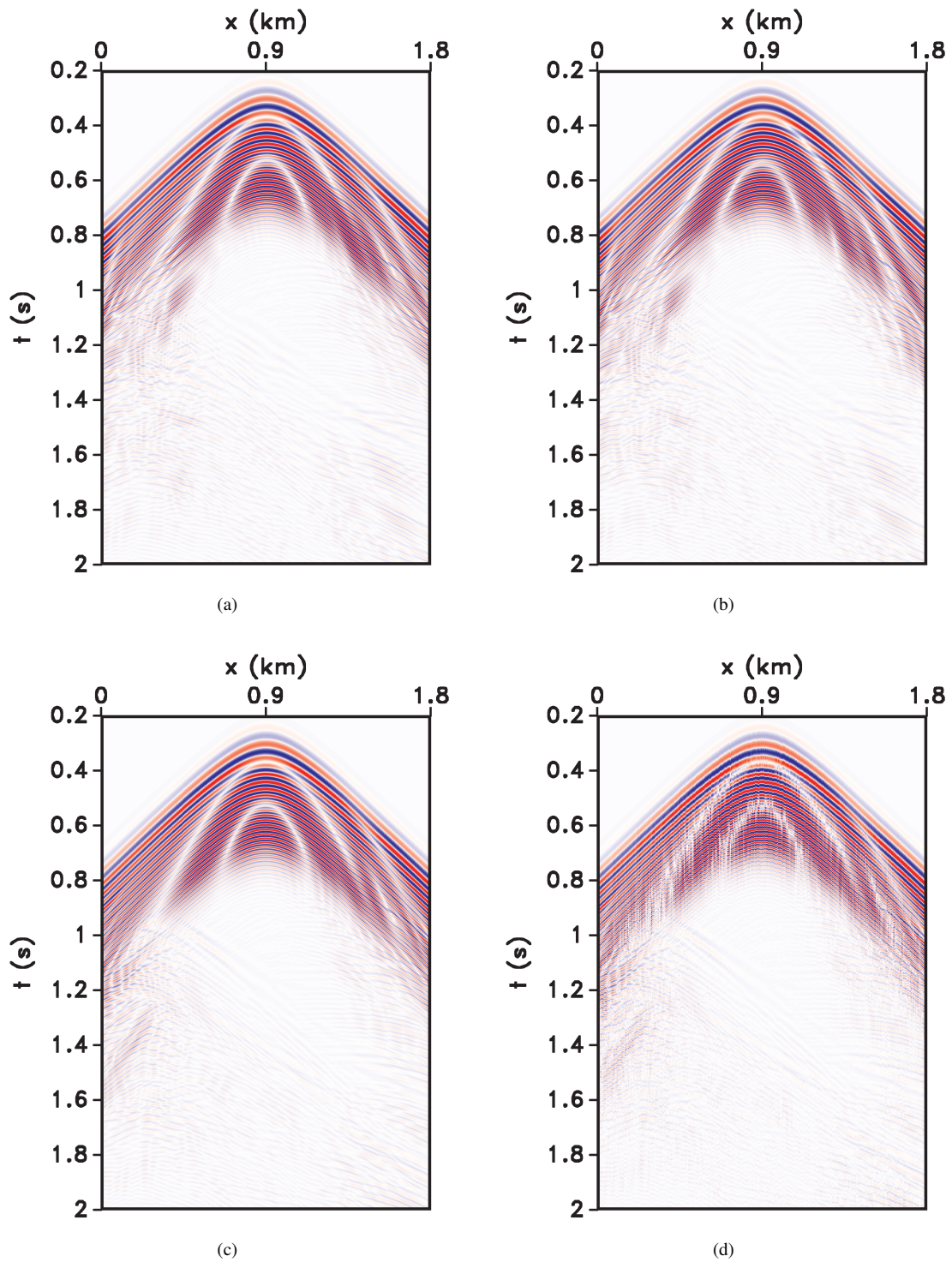
Figure 8. Shot gathers for (a) flat and (b) rough sea surface with ±5 m SWH, and receiver gathers for (c) flat and (d) rough sea surface with ±5 m SWH. The effects of a realistic rough sea surface are hardly noticeable in the shot gather domain, but easily noticeable in the receiver gather domain.

Guitton, A., B. Duquet, S. Secker, J. P. Mascomere, and A. Feltham, 2021, A deconvolution-interpolation approach with sparse inversion to mitigate the Doppler effect in marine vibrators data: First international meeting for applied geoscience & energy, 2555–2559, doi:10.1190/segam2021-3593897.1.

Hampson, G., and H. Jakubowicz, 1995, The effects of source and receiver motion on seismic data: Geophysical Prospecting, **43**, no. 2, 221–244, doi:10.1111/j.1365-2478.1995.tb00133.x.

Hestholm, S., 1999, Three-dimensional finite difference viscoelastic wave modelling including surface topography: Geophysical Journal International, **139**, no. 3, 852–878, doi:10.1046/j.1365-246x.1999.00994.x.

Hestholm, S., and B. Ruud, 2002, 3D free-boundary conditions for coordinate-transform finite-difference seismic modelling: Geophysical Prospecting, **50**, no. 5, 463–474, doi:10.1046/j.1365-2478.2002.00327.x.

JafarGandomi, A., and S. Grion, 2021, Modelling of marine vibrator data: 82nd EAGE annual conference & exhibition, 1–5, doi:10.3997/2214-4609.202113202.

Komatitsch, D., F. Coutel, and P. Mora, 1996, Tensorial formulation of the wave equation for modelling curved interfaces: Geophysical Journal International, **127**, no. 1, 156–168, doi:10.1111/j.1365-246X.1996.tb01541.x.

Komatitsch, D., and J. P. Vilotte, 1998, The spectral element method: An efficient tool to simulate the seismic response of 2D and 3D geological structures: Bulletin of the Seismological Society of America, **88**, no. 2, 368–392, doi:10.1785/BSSA0880020368.

Konuk, T., and J. Shragge, 2020, Modeling full-wavefield time-varying sea-surface effects on seismic data: A mimetic finite-difference approach: Geophysics, **85**, no. 2, T45–T55, doi:10.1190/geo2019-0181.1.

Käser, M., and M. Dumbser, 2006, An arbitrary high-order discontinuous galerkin method for elastic waves on unstructured meshes—I. The two-dimensional isotropic case with external source terms: Geophysical Journal International, **166**, no. 2, 855–877, doi:10.1111/j.1365-246X.2006.03051.x.

Laws, R., D. Halliday, J.-F. Hopperstad, D. Gerez, M. Supawala, A. Özbek, T. Murray, and E. Kragh, 2019, Marine vibrators: the new phase of seismic exploration: Geophysical Prospecting, **67**, no. 6, 1443–1471, doi:10.1111/1365-2478.12708.

Laws, R., and E. Kragh, 2002, Rough seas and time-lapse seismic: Geophysical Prospecting, **50**, no. 2, 195–208, doi:10.1046/j.1365-2478.2002.00311.x.

Lipnikov, K., G. Manzini, and M. Shashkov, 2014, Mimetic finite difference method: Journal of Computational Physics, **257**, 1163–1227, doi:10.1016/j.jcp.2013.07.031.

Lisitsa, V., and D. Vishnevskiy, 2010, Lebedev scheme for the numerical simulation of wave propagation in 3D anisotropic elasticity: Geophysical Prospecting, **58**, no. 4, 619–635, doi:10.1111/j.1365-2478.2009.00862.x.

Liu, X., 2023, Modeling seismic waves in ocean with the presence of irregular seabed and rough sea surface: Journal of Geophysics and Engineering, **20**, no. 1, 49–66, doi:10.1093/jge/gxac093.

Marfurt, K. J., 1984, Accuracy of finite-difference and finite-element modeling of the scalar and elastic wave equations: Geophysics, **49**, no. 5, 533–549, doi:10.1190/1.1441689.

Martin, G. S., K. J. Marfurt, and S. Larsen, 2002, Marmousi-2: An updated model for the investigation of AVO in structurally complex areas: 72nd Annual International Meeting, SEG, Expanded Abstracts, 1979–1982, doi:10.1190/1.1817083.

Orji, O. C., W. Söllner, and L.-J. Gelius, 2012, Effects of time-varying sea surface in marine seismic data: Geophysics, **77**, no. 3, P33–P43, doi:10.1190/geo2011-0361.1.

Pierson, W. J., and L. Moskowitz, 1964, A proposed spectral form for fully developed wind seas based on the similarity theory of S. A. Kitaigorodskii: Journal of Geophysical Research, **69**, no. 24, 5181–5190, doi:10.1029/JZ069i024p05181.

Robertsson, J. O. A., R. Laws, C. Chapman, J. P. Vilotte, and E. Delavaud, 2006, Modelling of scattering of seismic waves from a corrugated rough sea surface: a comparison of three methods: Geophysical Journal International, **167**, no. 1, 70–76, doi:10.1111/j.1365-246X.2006.03115.x.

Schultz, P. S., A. W. Pieprzak, G. R. Johnson, and L. Walker, 1989, Simple theory for correction of marine vibroseis phase dispersion: 59th Annual International Meeting, SEG, Expanded Abstracts, 660–662, doi:10.1190/1.1889560.

Shragge, J., 2014, Solving the 3D acoustic wave equation on generalized structured meshes: A finite-difference time-domain approach: Geophysics, **79**, no. 6, T363–T378, doi:10.1190/geo2014-0172.1.

Shragge, J., and B. Tapley, 2017, Solving the tensorial 3D acoustic wave equation: A mimetic finite-difference time-domain approach: Geophysics, **82**, no. 4, T183–T196, doi:10.1190/geo2016-0691.1.

Smith, J. G., and M. R. Jenkerson, 1998, Acquiring and processing marine vibrator data in the transition zone: SEG Technical Program Expanded Abstracts 1998, Society of Exploration Geophysicists, 136–139, doi:10.1190/1.1820159.

Virieux, J., 1986, P-SV wave propagation in heterogeneous media: Velocity-stress finite-difference method: Geophysics, **51**, no. 4, 889–901, doi:10.1190/1.1442147.

Wolfram Research, Inc., 2021, Mathematica, Version 12.3: Champaign, IL.